Supplementary Information for

Atomic Resolution Imaging of Halide Perovskites

Yi Yu,[1,2] Dandan Zhang,[1,2] Christian Kisielowski,[3] Letian Dou,[1,2] Nikolay Kornienko,[1,2] Yehonadav Bekenstein,[1,2] Andrew B. Wong,[1,2] A. Paul Alivisatos,[1,2,4,5] & Peidong Yang[1,2,4,5]*

[1]Department of Chemistry, University of California, Berkeley, CA 94720, USA.

[2]Materials Sciences Division, Lawrence Berkeley National Laboratory, Berkeley, CA 94720, USA.

[3]The Molecular Foundry, Lawrence Berkeley National Laboratory, Berkeley, CA 94720, USA.

[4]Kavli Energy NanoScience Institute, Berkeley, California 94720, USA.

[5]Department of Materials Science and Engineering, University of California, Berkeley, CA 94720, USA.

* Corresponding author. E-mail: p_yang@berkeley.edu

Table of Contents

1. Synthesis of 2D Halide Perovskites

2. Characterizations

3. Image Processing & Simulations

4. First-principle Calculations

5. Stoichiometry of Layered Halide Perovsiktes

6. Electron Beam Damage

7. Choice of Accelerating Voltage and Imaging Mode

8. Low Dose-rate Imaging

9. Evaluation of Beam-induced Structure Change

10. Two Critical Points for The Low Dose-rate Holography Application

11. Coexistence of Cubic and Orthorhombic Phases

References & Figures S1-S13

1. Synthesis of 2D Halide Perovskites

Chemicals: Cs_2CO_3 (99.9%, Aldrich), octadecene (ODE, 90%, Aldrich), oleic acid (OA, 90%, Aldrich), $PbBr_2$ (99.999%, Alfa Aesar), oleylamine (OAm, Aldrich, 70%), hexane (99.9%, Fisher Scientific), all of the chemicals were used as received without further purification. Cs-oleate solutions were prepared via a reported approach developed by Protesescu *et al*(Ref. 2 in the main text). Briefly, 0.2 g Cs_2CO_3 and 0.6 mL OA were loaded into a 3-neck flask along with 7.5 mL ODE, degassed and dried under vacuum at 120 °C (all of the temperature mentioned in this section is referring to the temperature of the oil bath) for 20 min, and then heated under N_2 to 150 °C until all Cs_2CO_3 reacted with OA. 5 mL ODE and 0.2 mmol $PbBr_2$ were loaded into a 3-neck flask and degassed under vacuum for 20 min at 120 °C. 0.8 mL OAm and 0.6 mL OA were injected at 120 °C under N_2. The temperature was raised to 145 °C, waited for 20 min until the complete dissolution of the $PbBr_2$ salt. The solution was kept at 145 °C, and 0.7 mL of as-prepared Cs-oleate solution was quickly injected. After 4 - 5 hrs the reaction mixture was cooled by an ice-water bath. The NSs were isolated by centrifugation at 6000 rpm for 5 mins and washed once with hexane, the obtained precipitated nanoplates were re-dispersed in hexane for further use.

2. Characterizations

X-Ray Diffraction (XRD) was measured using a Bruker AXS D8 Advance diffractometer with a Cu K_α source. Atomic Force Microscopy (AFM) images of the thin sheets were taken using an Asylum MFP 3D in tapping mode. Grazing Incidence Wide Angle X-Ray Scattering (GIWAXS) spectra were taken at beamline 7.3.3. at the Advanced Light Source (ALS) at Lawrence Berkeley National Lab utilizing an incident wavelength of 10 keV. 2D spectra were recorded with a Pilatus 2M-2D detector and integrated to reduce to 1D with NIKA GIWAXS software. Low magnification transmission electron microscopy (TEM) and high angle annular dark-field scanning transmission electron microscopy (HAADF-STEM) images, as well as the energy dispersive X-Ray spectroscopy (EDS) were acquired using a FEI Titan 60-300 microscope. The aberration-corrected high-resolution TEM (AC-HRTEM) images were collected using the negative spherical aberration (C_S) imaging (NCSI) technique(Refs. 8 & 22 in the main text) on the TEAM 0.5 microscope, which is an aberration-corrected microscope equipped with a high-brightness Schottky-type field emission gun and a Wien-filter monochromator[1]. Aberration-corrected HRSTEM (AC-HRSTEM) images were also acquired on TEAM 0.5 in the STEM mode. The accelerating voltages were chosen to be 80 kV and 300 kV, respectively, for the compared experiments. The optimum voltage for low dose AC-HRTEM was chosen as 80 kV. The lens aberrations were measured and compensated prior to the image acquisition by evaluating the Zemlin tableau of an amorphous carbon area close to the area of interest in the specimen. In order to rule out the possible effect of microscope instability, we measured the residual aberrations before and after our imaging experiment and checked it every 2 hours in between. No obvious changes of these parameters could be found, confirming the reliability of our experimental data. According to the measurements, the residual lens aberrations were listed below: $C_S \sim$ -9 μm, two-fold astigmatism $A1 <$ 2 nm, three-fold astigmatism $A2 <$ 30 nm, axis coma $B2 <$ 30 nm.

3. Image Processing & Simulations

To avoid any possible artifact, we insist on using the original image data for interpretation. All the images in the main text and supplementary information are presented as they were acquired, except for Fig. 3a. Fig. 3a is a single-shot AC-HRTEM image with medium dose. The background of the amorphous carbon supporting film introduces unwanted noise to the image. To remove the effect of this noise, the original image was Fourier-filtered. The masking area was chosen such that all the fundamental spots and related streaks were fully maintained. Detailed method and evaluation of the filtering effect are provided elsewhere(Refs. 10 & 22 in the main text). The estimation of the thickness of the NS in Fig. 3a was done by comparing to the simulation result (Fig. S11). In Fig. 1c, Fig. 2d and 2e, the brightness and contrast were adjusted to provide a better display in the print version. All quantitative analyses of those images (Fig. 1, 2) were performed using the original data. Before quantitative measurements were carried out in Fig. 4, scale bars of the experimental images have been carefully calibrated using a single layer graphene sample (Fig. S12). Exit-wave reconstruction (EWR) and image simulation were carried out using MacTempas software[2]. EWR was based on the Genchberg-Saxton algorithms[3](also see Ref. 21 in the main text), and for image simulation, the multislice method[4] was used. For simulation of the phase images, we first simulated a series of images with different focus values. These images were simulated under similar microscope operation conditions as in the experiments. In order to get closer to the experimental data, 5% white noise was added to the simulated images. Afterwards, the same EWR process was conducted and the simulated exit-wave was obtained. Finally, the simulated phase image was extracted from the simulated, complex exit-wave function. Structure models shown in this work were drawn using the VESTA software[5].

4. First-principle Calculations

First-principle calculations based on the density-functional theory (DFT), were performed using the ABINIT code[6]. For the exchange and correlation functional, the generalized gradient approximation (GGA) proposed by Perdew, Burke, and Ernzerhof (PBE) was used[7]. The electronic wave functions were expanded via a plane-wave basis set with a cutoff energy of 20 Hartree. The equilibrium lattice constants were obtained by a full optimization of the unit cell. The structural relaxations were carried out until the residual forces were less than 2.5×10^{-3} eV/Å.

5. Stoichiometry of Layered Halide Perovsiktes

Layered halide perovskites have a general formula of $A_{m+1}B_mX_{3m+1}$, where A and B are A-site and B-site cations, respectively, and X is a halide. The variable m indicates the number of layers. In the extreme case where $m = \infty$, the stoichiometry becomes ABX_3 and the structure is a three-dimensionally bonded bulk perovskite. In the opposite extreme, for example, mono- and double-layer $CsPbBr_3$, where m = 1, and 2, respectively, the stoichiometries become Cs_2PbBr_4, and $Cs_3Pb_2Br_7$, respectively. All the

discussions and simulations for layered structures in this manuscript are based on these layer-specific stoichiometries.

6. Electron Beam Damage

In TEM, the electron irradiation effects are mainly considered as knock-on damage, radiolysis damage, and e-beam heating[8-10]. Knock-on damage, corresponding to the atom displacements, is attributed to the inelastic scattering of electrons at *nuclei*, and this process dominates at high accelerating voltage. On the other hand, radiolysis damage, corresponding to ionization, is attributed to the inelastic electron scattering of an electron beam at *electrons* in the specimen, and this dominates at low accelerating voltage. The e-beam heating dominates in materials with poor thermal conductivity. Radiolysis damage has been well recognized in insulators, in which the localized electrons are sensitive to electronic damage. For metals, the presence of conduction electrons normally quenches electronic excitations within a short time so that the electronic damage should not occur, and the damage is attributed to a knock-on effect in that system. In terms of halide perovskites, the damage mechanism could be dominated by radiolysis as well as e-beam heating, as these materials are not good conductors for both electrons and heat. It seems that higher accelerating voltage may help to eliminate the damage. However, the phenomenon of e-beam induced Pb precipitates in Pb-contained oxide perovskites is also well known for TEM experiments at high voltage. Therefore, there is no simple rule to follow, and we believe the best way to handle samples with these materials is to do comparative experiments at both low and high accelerating voltages.

7. Choice of Accelerating Voltage and Imaging Mode

We have tested our samples with different imaging modes (TEM *vs.* STEM) and at both low (80 kV) and high (300 kV) accelerating voltages. The results are shown in Fig. S3. Here, the samples were first illuminated at high magnifications using traditional illumination doses and rates, and then images were taken at lower magnifications to reveal the entire morphology of the NSs. It can be seen that the NSs were quickly damaged in all the cases, regardless of whether the damage mechanism is governed by radiolysis (at lower voltage) or knock-on (at higher voltage) damage. We assume that the ultrathin nature of the 2D $CsPbBr_3$ NSs makes them susceptible to damage because binding energies are lowered in surface proximity.

From the morphology of the damage, it can be observed that the major products caused by beam damage are nanoparticle-precipitates, which appear as dark dots in TEM (Figs. S3a and S3b) and as bright dots in STEM (Figs. S3c and S3d). Detailed analysis of the damaged products was carried out using AC-HRTEM and AC-HRSTEM. The results are shown in Fig. S4. A HRSTEM image of the edge of a damaged NS is depicted in Fig. S4a. Voids and nanoparticle-precipitates can be observed. One of the nanoparticles (indicated by red box) is enlarged to show in Fig. S4b and the corresponding Fourier transform (FT) is shown in Fig. S4c. It is clear from the indexed result that the nanoparticle should be Pb with a typical face-centered-cubic (FCC) structure. The same result is also demonstrated in the AC-HRTEM image (red boxed region in Fig. S4d) and the corresponding FT (Fig. S4f). As lots of Pb nanoparticles precipitate, it is intuitive to

consider that the regions nearby could be Pb-deficient products. This is evidenced by the analysis from Fig. S4e, where the remaining region (indicated by blue box) surrounded by Pb nanoparticles is analyzed to be a Pb-deficient phase of CsBr.
From Fig. S3, we can also see the damage is different at different voltage. In 300 kV TEM the precipitates are in surface proximity. One expects this behavior from displacement damage, which depends on binding energies[11]. At 80 kV, the precipitates are larger, which points towards Oswald ripening and requires sample heating/ionization[12].
Since the NSs could be easily damaged in all the cases, we have to choose a slower damaging mode to explore the possibility of atomic-scale imaging. Firstly, comparing the imaging mode, we found that samples were normally damaged quicker under the STEM mode, which uses a converged electron beam. Besides, a converged STEM beam could easily induce voids in the samples. Moreover, as STEM is more sensitive to the surface contamination than TEM, the possible surface ligands or absorptive surface contamination blurred the STEM images in most cases, especially for HRSTEM images. Therefore, we prefer TEM mode to further explore the atomic resolution imaging. Secondly, in terms of accelerating voltage, we choose 80 kV instead of 300 kV. The choice of lower voltage is critical as it can provide higher contrast, which is quite helpful for locating samples at low magnifications under the dim low-dose beam, which will be detailed in the following section.

8. Low Dose-rate Imaging

As mentioned before, the beam-sensitive nature of halide perovskites hinders atomic-scale imaging. Therefore, we explore decreasing the electron dose-rate, which is an emerging technique that retards damage[13,14](also see Ref. 15 in the main text). However, a very low dose-rate could make the images so noisy that useful information is difficult to extract. As described in the main text, we applied EWR to overcome the noise problem. The detailed experimental setup for low dose-rate imaging is provided below.
2D $CsPbBr_3$ NSs were drop-casted on either ultrathin (< 3 nm) carbon supporting membranes or graphene supporting membranes (Ted Pella). The usage of the ultrathin supporting membrane minimizes the background noise. The beam-illumination area and electron dose-rate were controlled using the monochromator caustic with a bar-shape slit aperture. The slit aperture ensures the illuminated area only is confined within the aperture, and shifting different parts of the monochromator illumination onto the camera allows for changing dose-rates by orders of magnitude[13,14]. In order to obtain the pristine atomic structure, we carefully handled the sample to avoid unnecessary beam exposure. For locating the NSs, we only imaged at very low magnification with decreased dose-rate. The beam is extremely dim such that we could just able to see the weak contrast from the squared NSs. The dose-rate used for locating the samples was less than 10 $eÅ^{-2}s^{-1}$. The usage of lower voltage (80 kV) is important here for contrast enhancement. In opposite case, at 300 kV, we could not see the NSs (as they were quite transparent) at low magnification with low dose unless a large defocus was applied. We searched for the NSs by randomly moving the sample. Once the NSs were found, we quickly shifted the NS of interest outside the illuminated region. Afterwards, we increased the magnifications and tuned all the imaging parameters (dose-rate, objective stigmation, etc.) in the nearby

supporting membrane region. When we were ready for imaging, we shifted the sample in such a direction that the NS of interest moved back towards the camera, i.e., the illuminated region. Once the edge of the NS came into the view, we began to acquire either a single-shot AC-HRTEM image or a focal-series of AC-HRTEM images for a posteriori EWR, which provides an in-line hologram with separated amplitudes and phases. We believe such a low dose-rate imaging procedure better protects the pristine structure of any sample from beam damage[15]. We have also evaluated the electron-sample interaction under such circumstances as discussed in the following section.

9. Evaluation of Beam-induced Structure Change

Even under the low dose conditions, it is still important to evaluate the possibility of beam-induced structural changes so that one can know what is the pristine structure and what is caused by the electron beam. To check for beam-induced structural changes, we propose two methods for two different cases.

First, if the dose-rate is not too low such that structural details can still be distinguished in individual HRTEM images, as the case in Fig. S5, we can directly compare sequential images one by one. If there is no obvious change (atomic displacements, disappearance of atoms, etc.) all across the whole focal-series, then it is reasonable to claim that the material can maintain its pristine structure within the focal-series. Otherwise, if structural change can be detected at a certain step, then only the focal-series images before this step are considered safe to be used for reconstruction. The images after the step are not suitable to be used for the characterization of the pristine structure.

Second, if the dose-rate is too low to see structural details in individual HRTEM images, such as when the dose-rate is lower than 10 $eÅ^{-2}s^{-1}$, then we can divide the focal-series into several sub-series and compare the reconstructed amplitude/phase images from each sub-series. Similarly, if no structural change can be traced among these reconstructions, then we can rule out the electron beam effect. Otherwise we have to discard that part of the dataset. This method can also be applied to the first case as well.

We have applied the above methods to check our data and ensured that the examples we presented here (Figs. 1, 2, Figs. S5 and S9) are indeed an accurate representation of the pristine crystal structure.

10. Two Critical Points for The Low Dose-rate Holography Application

1. Accumulating a large amount of dose over a long period of time does not equal to accepting large amount of dose over one short time.

This is in agreement with measurements at lower magnifications by van den Berg *et al*[16]. This effect makes our imaging method feasible. For example, as the case in Fig. S5, one may notice that although low dose-rate ~ 100 $eÅ^{-2}s^{-1}$ was applied, the total focal-series of 80 images (80 s exposure) accumulated a total dose of ~ 8000 $eÅ^{-2}$. As can be seen from sequential images from Fig. S5a, no structural damage could be observed. However, exposing the samples to ~ 10^4 $eÅ^{-2}$ electrons in single HRTEM image (dose-rate of 10^4 $eÅ^{-2}s^{-1}$, exposure time 1 s) damages the NS.

2. The critical dose-rate for a specific sample should be experimentally evaluated.

When applying this method for imaging beam-sensitive materials, it is necessary to determine the critical dose-rate for the specific sample with a specific thickness. For our 2D $CsPbBr_3$ NSs, we have varied the dose-rate from ~ 10 $eÅ^{-2}s^{-1}$ to ~ 500 $eÅ^{-2}s^{-1}$. We found that no obvious damage (such as Pb precipitation) had occurred for all the cases. However, surface atom movements may become obvious when the dose-rate is larger than 200~300 $eÅ^{-2}s^{-1}$. Even in the case of Figs. 1, 2 and Fig. S5, electron sputtering of the outmost surface atoms exists. This can explain the lower phase values in the outmost two atomic layers of atoms in Fig. 2a. Therefore, this dose-rate is safe to image the "bulk feature" of the NS, but not suitable to image the surface atom steps. If one is interested in the surface atomic steps of theses 2D NSs, then the suitable dose-rate should be used is ~10 $eÅ^{-2}s^{-1}$ for this sample. However, lower dose-rates require the acquisition of more images to maintain a desired signal-to-noise ratio in the reconstruction. In summary, it is a compromise to choose a suitable dose-rate and number of images. The choice of low dose imaging parameters depends on the robustness of the imaged object and the specific imaged area (bulk study or surface study).

11. Coexistence of Cubic and Orthorhombic Phases

The outstanding advantage of the outlined TEM analysis is that the crystal structure of 2D $CsPbBr_3$ NSs can be analyzed locally sheet-by-sheet, so that in principle, the structure of each NS can be obtained, which is different from the ensemble information obtained by XRD. We have tested dozens of NSs, and it is found that many of the NSs present a cubic structure while some of them show orthorhombic domains.

Fig. S9a shows the atomically resolved phase image of a 2D $CsPbBr_3$ NS obtained by reconstructing 70 low dose-rate (dose-rate ~70 $eÅ^{-2}s^{-1}$) AC-HRTEM images. Its Fourier transform provides the local nano-diffraction pattern that reveals the orthorhombic structure of $CsPbBr_3$. The orthorhombic characteristic spots are highlighted by red circles in Fig. S9b. Tilting of octahedrons can be directly observed. By checking all the images within the focal series, we confirm that the orthorhombic phase is stable under the dose-rate of ~70 $eÅ^{-2}s^{-1}$.

Apart from Fig 3 and Fig 4, Fig. S9d shows another example of coexistence of cubic and orthorhombic $CsPbBr_3$ within a single NS, using the in-line holography method. The atomically resolved phase image is obtained by reconstructing 26 AC-HRTEM images (dose-rate ~480 $eÅ^{-2}s^{-1}$) via exit-wave reconstruction. The corresponding 2D phase mapping is depicted in Fig. S10. In Fig. S9d, the upper left region shows the cubic structure without octahedron tilting, while the lower right region shows the orthorhombic structure with obvious octahedron tilting.

It is noticed that the tilting angle of octahedrons (defined as in Fig. 4) in Fig. S9 is smaller than the case presented in Fig. 3 and Fig. 4, which suggests the suppression of octahedron tilting could occur in some NSs. This is supposed to be related with the 2D feature of the NSs. Without strong 3D bonding, the lattice distortion/octahedron tilting is relaxed to some extent. To further explore the suppression of octahedron tilting, comparisons between more NSs and different regions (center vs. edge) are needed for future work.

It is important to evaluate the possibility of beam-induced phase change here. We can rule out the possibility of a beam-induced formation of the orthorhombic structure by

deliberately exposing the cubic NSs to the electron beam, and none of the cubic NSs could be converted into orthorhombic structure by this method. Vice versa, for the orthorhombic to cubic structure transformation, in principle, it can occur once the beam-induced heating causes the temperature to rise to the phase transition point of 403 K. However, under the low voltage and low dose-rate imaging conditions, it seems impossible to induce elevated temperature more than 100 K[8]. Experimentally, we did observe the orthorhombic structure could be stable under lower dose-rates as demonstrated in Fig. S9a. However, with higher dose-rates ($\geq$ 500 $e\text{Å}^{-2}s^{-1}$) and longer exposure time, sometimes the orthorhombic region could be observed to convert into cubic phase. For example, in the case of Fig. S9d, we found that the orthorhombic region began to transform into cubic structure after the acquisition of 26 images, so that we only used first 26 images for reconstruction of the image demonstrating the initial existence of the orthorhombic phase. According to our imaging experiments on many few-layer $CsPbBr_3$ NSs, it is found that the dose-rate of 100 $e\text{Å}^{-2}s^{-1}$ or less is safe to maintain the pristine structure. Therefore, the cubic and orthorhombic structure observed could be the as-synthesized phases.

The phenomenon of coexistence of two phases may be understood from the energetic point of view. In the Ref. 2 in the main text, the energy per formula unit of cubic and orthorhombic $CsPbBr_3$ was calculated using DFT. The energy difference of the two polymorphs is 0.07 eV, much lower than the case of $CsPbI_3$ (0.18 eV). Here, we have also verified via our DFT calculations using a different code. The calculated energy difference between cubic and orthorhombic $CsPbBr_3$ is 0.27 eV, still lower than the case of $CsPbI_3$ (0.38 eV). Therefore, both calculation results indicate that, for $CsPbBr_3$, the energy barrier between cubic and orthorhombic polymorphs is typically lower than the case of other halide-group perovskites (e.g. $CsPbI_3$), which can support the observed coexistence of two phases in $CsPbBr_3$.

References

1. Kisielowski, C. *et al*. Detection of single atoms and buried defects in three dimensions by aberration-corrected electron microscope with 0.5-angstrom information limit. *Microsc. Microanal.* **2008**, 14, 469–477.
2. Kilaas, R. MacTempasX. http://www.totalresolution.com (accessed May 23, 2015).
3. Gerchberg, R. W.; Saxton, W. O. A pratical algorithm for the determination of phase from image and diffraction plane pictures. *Optik* **1972**, 35, 237-246.
4. Cowley, J. M. *Diffraction Physics*. (Elsevier, Amsterdam, 1995).
5. Momma, K.; Izumi, F. VESTA 3 for three-dimensional visualization of crystal, volumetric and morphology data. *J. Appl. Cryst.* **2011**, 44, 1272-1276.
6. Gonze, X. *et al*. ABINIT: First-principles approach to material and nanosystem properties. *Comput. Phys. Commun.* **2009**, 180, 2582-2615.
7. Perdew, J. P.; Burke, K.; Ernzerhof, M. Generalized gradient approximation made simple. *Phys. Rev. Lett.* **1996**, 77, 3865-3868.
8. Egerton, R. F.; Li, P.; Malac, M. Radiation damage in the TEM and SEM. *Micron* **2004**, 35, 399-409.
9. Egerton, R. F. Choice of operating voltage for a transmission electron microscope. *Ultramicroscopy* **2014**, 145, 85-93.

10. Banhart, F. "Electron and ion irradiation" in In-situ Electron Microscopy: Applications in Physics, Chemistry and Materials Science, Dehm, G., Howe, J. M., Zweck, J., Eds. (Wiley-VCH Verlag GmbH & Co. KGaA: Weinheim, 2012), pp. 125-143.
11. McKinley, W. A.; Feshbach, H. The Coulomb scattering of relativistic electrons by nuclei. *Phys. Rev.* **1948**, 74, 1759-1763.
12. Simonsen, S. B.; Chorkendorff, I.; Dahl, S.; Skoglundh, M.; Sehested, J.; Helveg, S. Direct observations of oxygen-induced platinum nanoparticle ripening studied by in situ TEM. *J. Am. Chem. Soc.* **2010**, 132, 7968-7975.
13. Barton, B.; Jiang, B.; Song, C.; Specht, P.; Calderon, H.; Kisielowski, C. Atomic resolution phase contrast imaging and in-line holography using variable voltage and dose rate. *Microsc. Microanal.* **2012**, 18, 982-994.
14. Kisielowski, C.; Specht, P.; Gygax, S. M.; Barton, B.; Calderon, H. A.; Kang, J. H.; Cieslinski, R. Instrumental requirements for the detection of electron beam-induced object excitations at the single atom level in high-resolution transmission electron microscopy. *Micron* **2015**, 68, 186-193.
15. Kisielowski, C. Observing atoms at work by controlling beam-sample interactions. *Adv. Mater.* **2015**, 27, 5838-5844.
16. van den Berg, R.; Elkjaer, C. F.; Gommes, C. J.; Chorkendorff, I.; Sehested, J.; de Jongh, P. E.; de Jong, K. P.; Helveg, S. Revealing the formation of copper nanoparticles from a homogeneous solid precursor by electron microscopy. *J. Am. Chem. Soc.* **2016**, 138, 3433-3442.

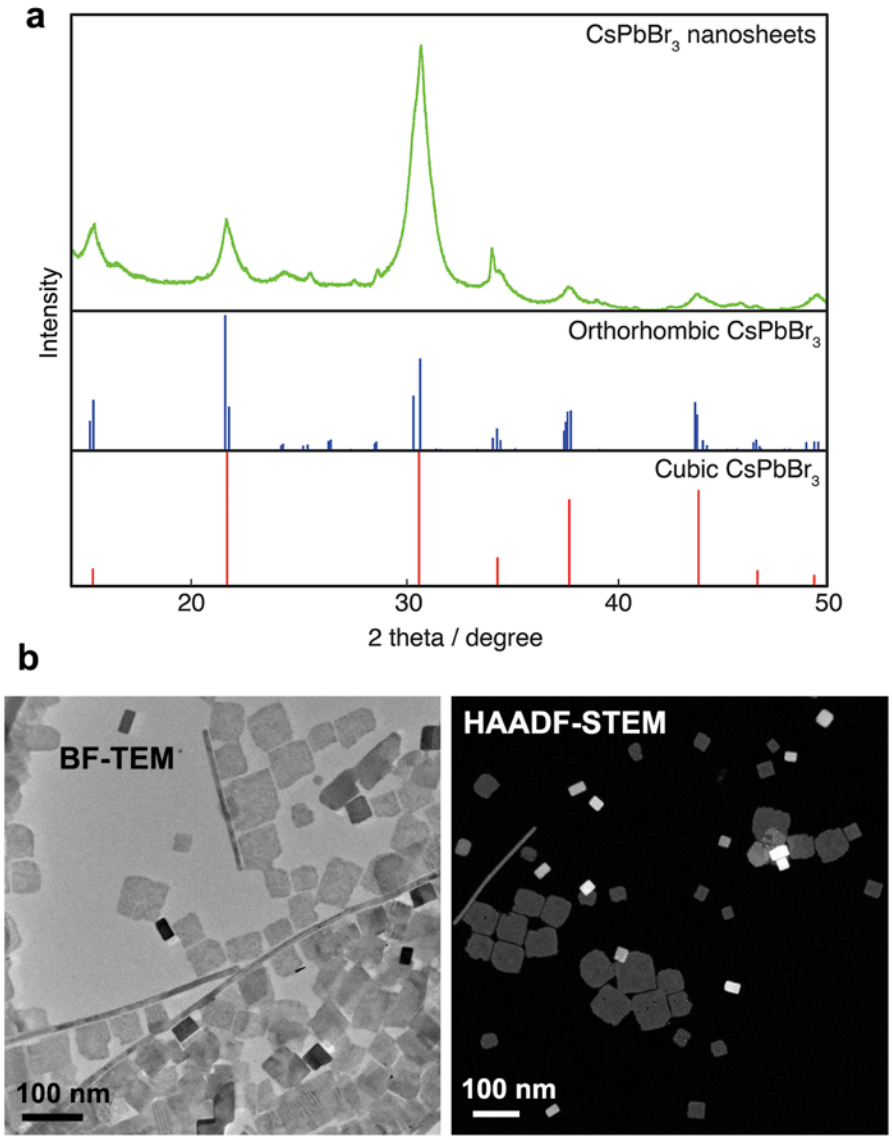

Figure S1. XRD and Low magnification S/TEM of 2D $CsPbBr_3$ NSs. (a) XRD of 2D $CsPbBr_3$ NSs. The standard XRD patterns of orthorhombic and cubic phases are also provided for comparison. (b) Low magnification bright field-TEM and HAADF-STEM images of 2D $CsPbBr_3$ NSs. The main products are 2D NSs while there are some by-products of nanowires and nanocubes. In the STEM image, 2D NSs show weak contrast compared to the bright contrast of nanocubes, indicating the ultrathin feature of these NSs.

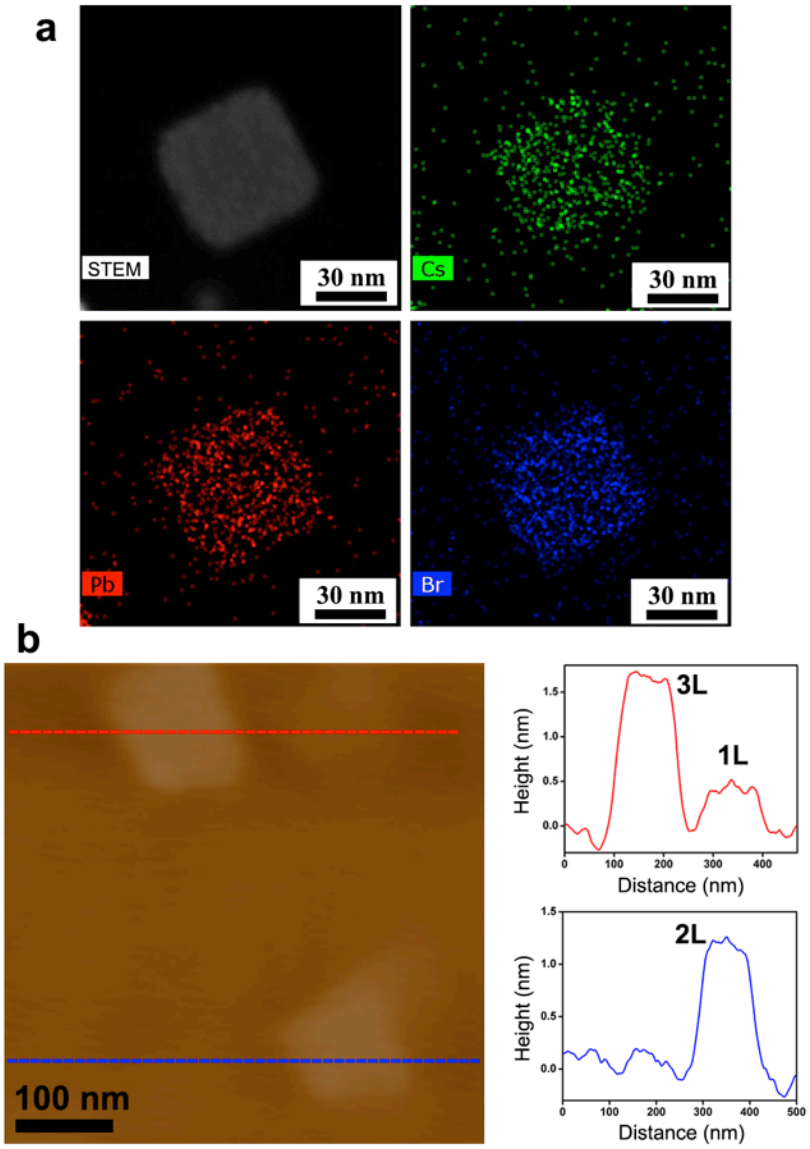

Figure S2. STEM-EDS mapping and AFM images of 2D $CsPbBr_3$ NSs. (a) STEM-EDS mapping of single 2D $CsPbBr_3$ NS. The components of Cs, Pb, and Br are confirmed, and their distribution is homogeneous across the whole NS. Due to the ultrathin feature of the NSs, EDS mapping was obtained via multiple scans in order to accumulate a sufficient amount of signal. The STEM image shown here is the image acquired at the first scan. Then the sample was gradually damaged during multiple scans, and we stopped the scanning before serious damage occurred. (b) AFM image of three $CsPbBr_3$ NSs and the corresponding line profiles. The thickness of the NSs is 3-layer, 1-layer, and 2-layer, respectively.

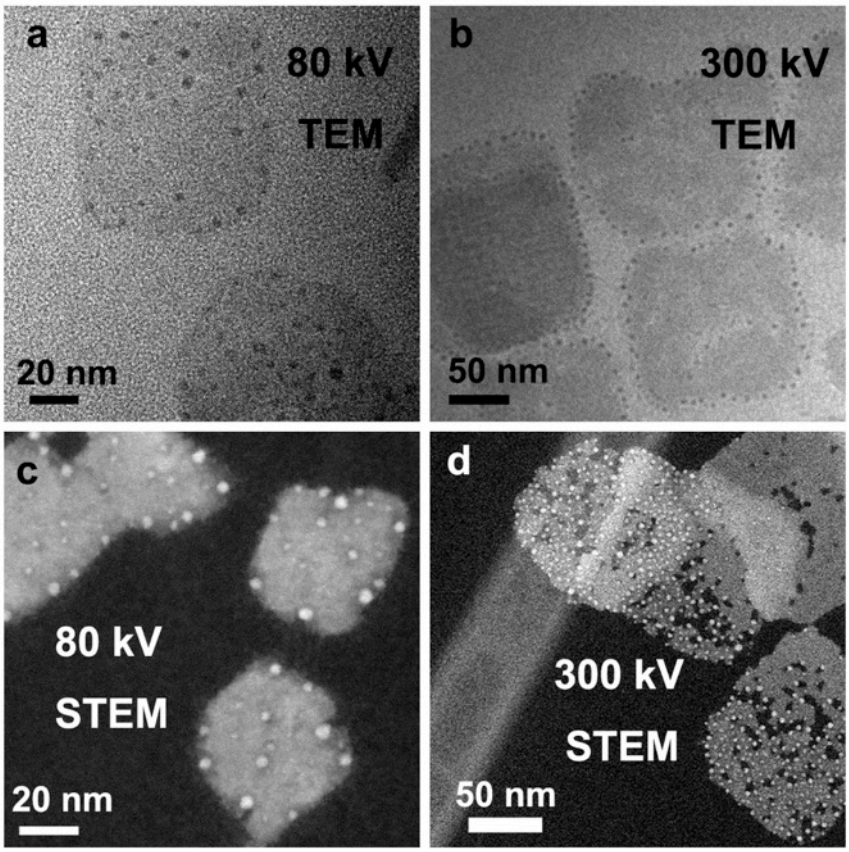

Figure S3. $CsPbBr_3$ NSs images acquired at different accelerating voltages (80 kV *vs.* 300 kV) and different imaging modes (TEM *vs.* STEM). For TEM images, the samples were first illuminated at high magnifications with conventional HRTEM dose-rate of ~ 10^4-10^5 $eÅ^{-2}s^{-1}$, and then imaged at lower magnifications as shown in (a) and (b). Similar process was also applied in the STEM cases. $CsPbBr_3$ NSs were easily damaged in all the cases. Detailed imaging conditions for (a-d) are provided below. (a) dose-rate: ~10 $eÅ^{-2}s^{-1}$, exposure time 1 s. (b) dose-rate: ~5 $eÅ^{-2}s^{-1}$, exposure time 1 s. (c) dose-rate: ~10^8 $eÅ^{-2}s^{-1}$, dwell time 12 μs. (d) dose-rate: ~10^7 $eÅ^{-2}s^{-1}$, dwell time 3 μs.

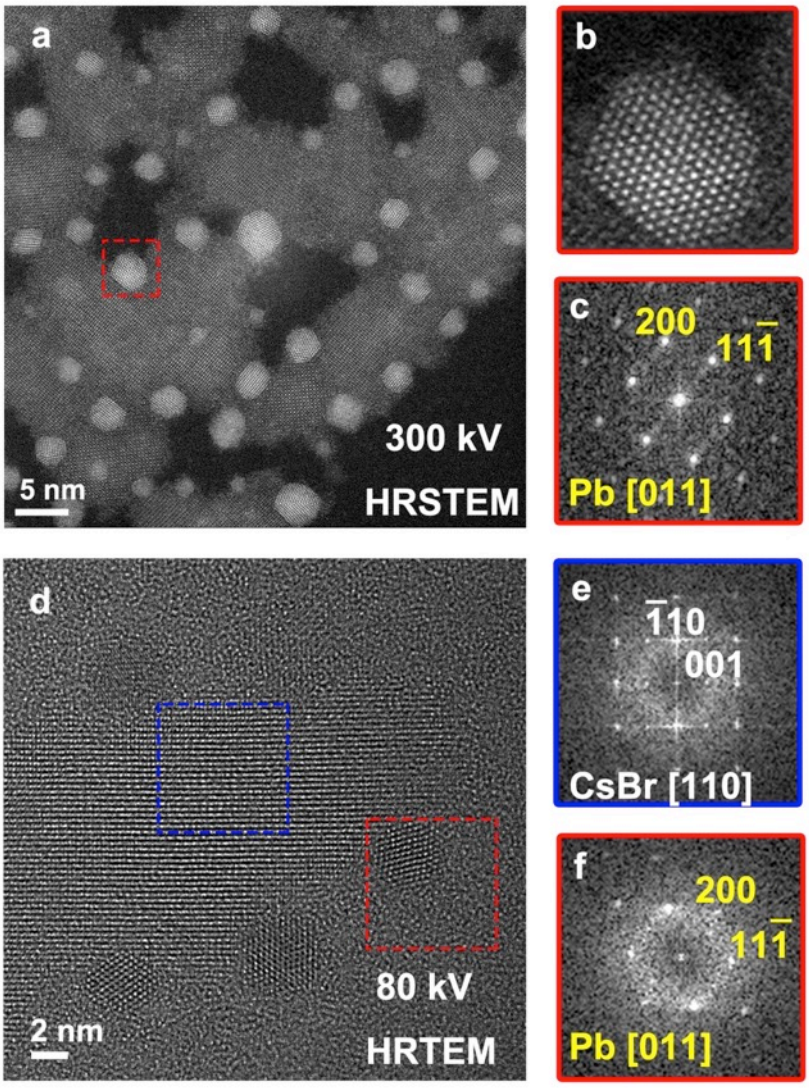

Figure S4. Analysis of the products caused by electron beam damage by AC-HRSTEM and AC-HRTEM. (a) AC-HRSTEM image acquired at 300 kV. One of the nanoparticle-precipitates is boxed, and the enlarged image and corresponding FT are shown in (b) and (c), respectively. The precipitates are determined to be Pb FCC nanoparticles. The same result is also obtained in AC-HRTEM analysis (d). (e) and (f) are FTs of the regions as indicated by blue box and red box, respectively. The precipitates are indexed to be Pb and the rest materials become a Pb-deficient product, i.e. CsBr. (a) and (d) were acquired on the regions where beam damage had occurred beforehand. The imaging parameters are: (a) dose-rate: ~10^9 e$Å^{-2}s^{-1}$, dwell time 3 μs. (d) dose-rate: ~500 e$Å^{-2}s^{-1}$, exposure time 1 s.

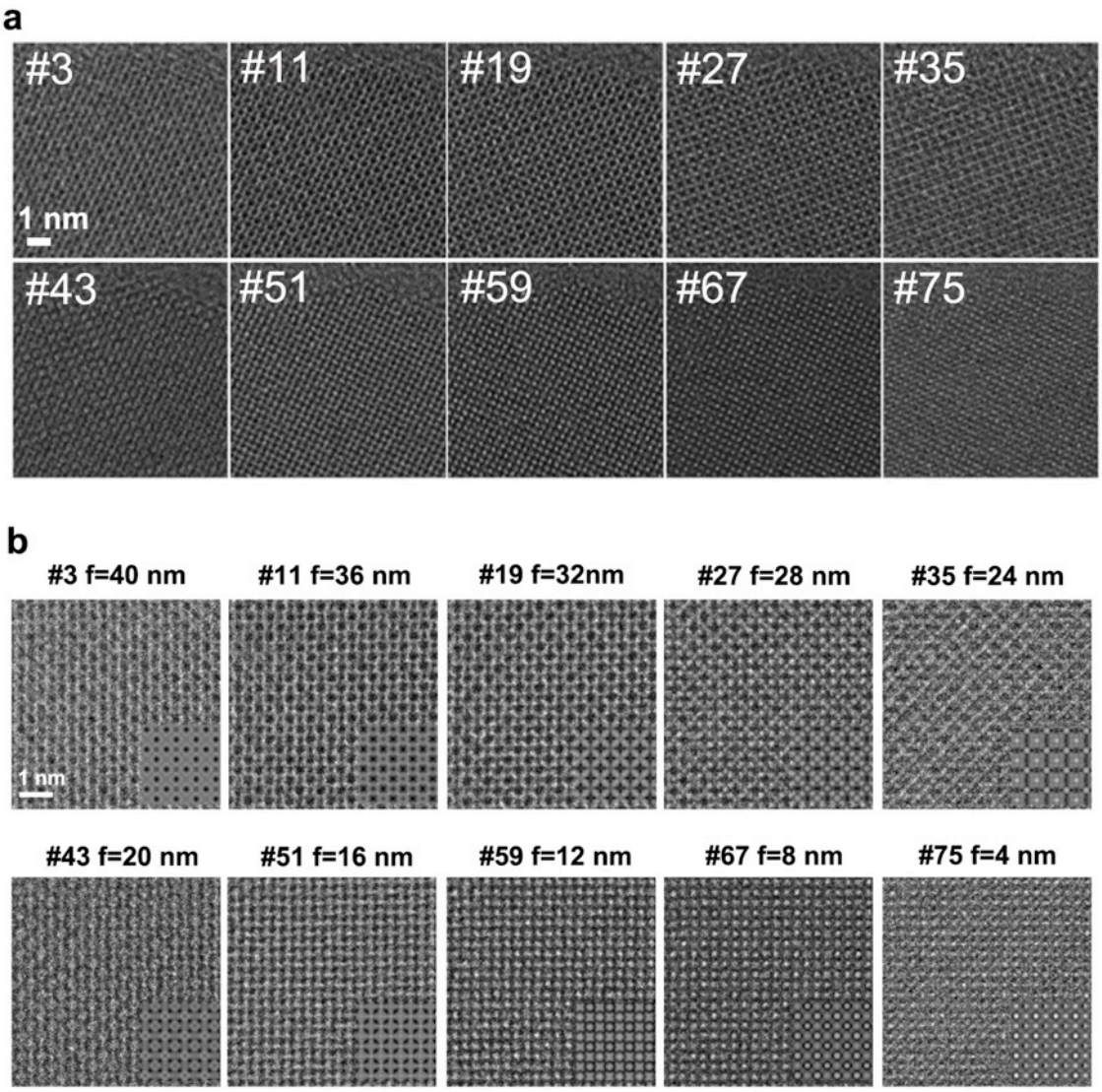

Figure S5. AC-HRTEM images from a focal-series of 80 images. (a) AC-HRTEM images from a focal-series of 80 images. The starting focus is around 40 nm and the focus step is -0.5 nm. The dose-rate is ~100 $eÅ^{-2}s^{-1}$, and the NS is robust under this low dose-rate condition. There is no observable beam-induced structural change within all 80 images. Image delocalization occurred at large defocus. (b) Enlarged experimental AC-HRTEM images and corresponding simulated images (overlaid on the lower right region). Qualitatively, experimental images agree well with the simulation using a 2-layer model.

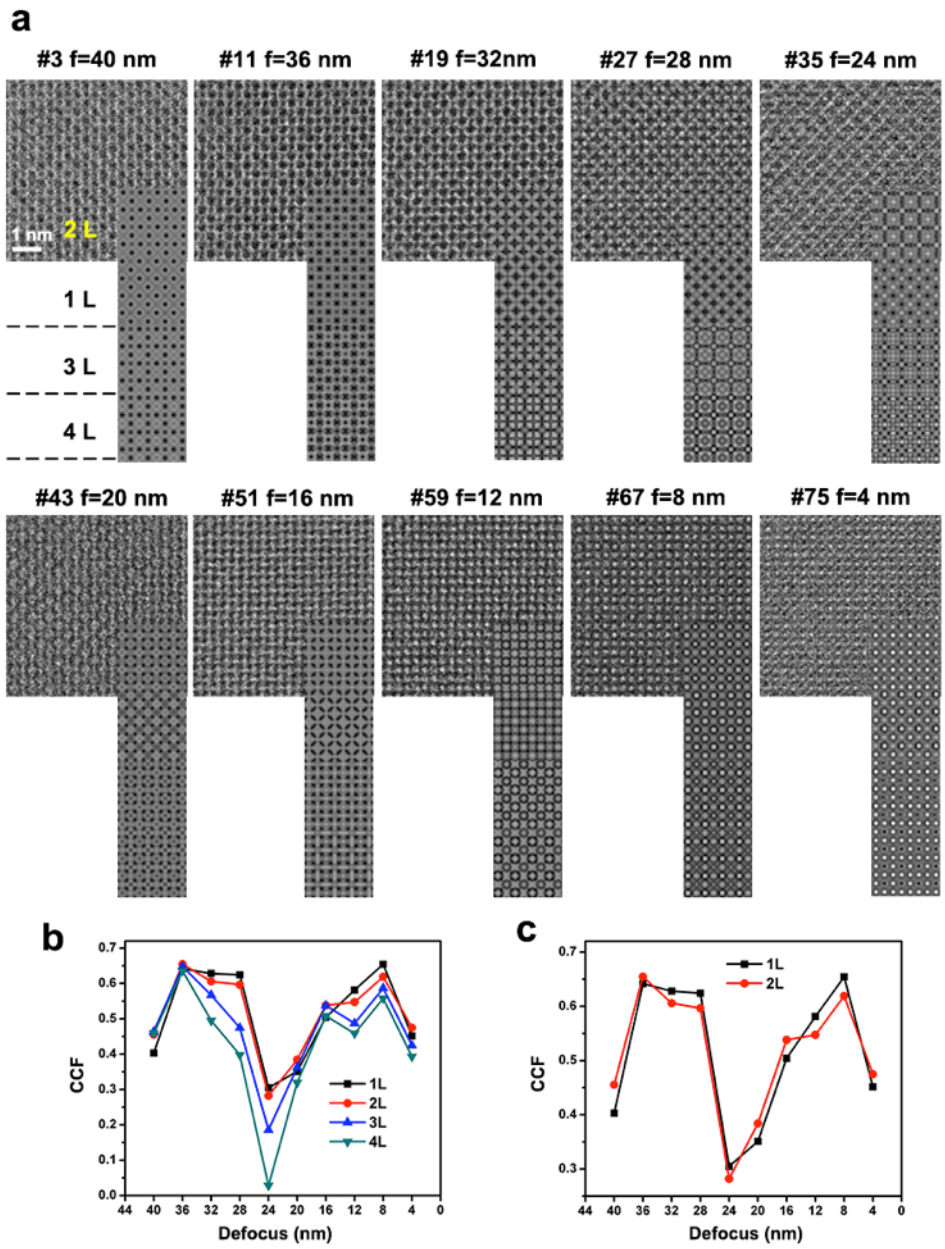

Figure S6. Comparison of experimental images with simulated images from 1-layer to 4-layer. (a) Simulations with 2-layer thickness are overlaid on the lower right corner of the experimental images, the same as in Fig. S5b. Simulations of 1-layer, 3-layer, and 4-layer are provided in parallel. (b) Quantitative measurement of the similarity between experimental and simulated images using cross-correlation coefficient (CCF). It is obvious that 1- and 2- layers have higher CCF compared to 3- and 4- layers. (c) Enlarged comparison of CCF between 1- and 2- layers. Among all 10 images, 1-layer model fits better with experiments in 5 images while 2-layer model fits well with the other 5 images. The overall characteristics between 1- and 2- layers are similar. To unequivocally determine the thickness, complementary phase information (Figs. 2, S8) is needed.

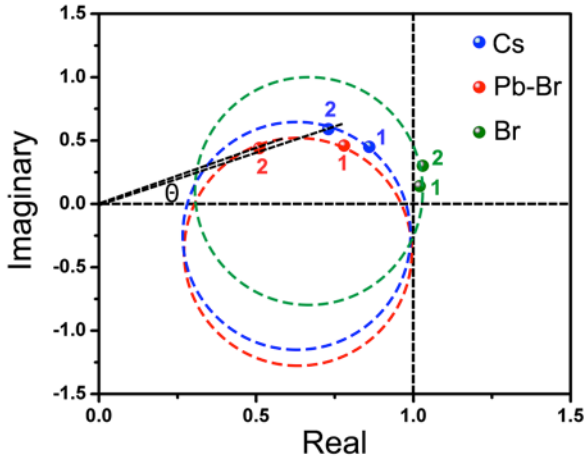

Figure S7. Argand plots for 1-layer and 2-layer $CsPbBr_3$ obtained from simulated exit-waves. Blue, red, and green data points represent Cs columns, Pb-Br columns, and Br columns, respectively. The numbers 1 and 2 indicate the data points from 1-layer exit-waves and 2-layer exit-waves, respectively. The circles schematically show the locus of the data points from different columns as the mass/thickness increases. The phase is characterized by the angle θ between any data point and the incident/vacuum wave at (1,0). In the 2-layer case, the measured phase of Pb-Br column is slightly larger than the Cs column, which is in agreement with our experimental measurements as described in the main text.

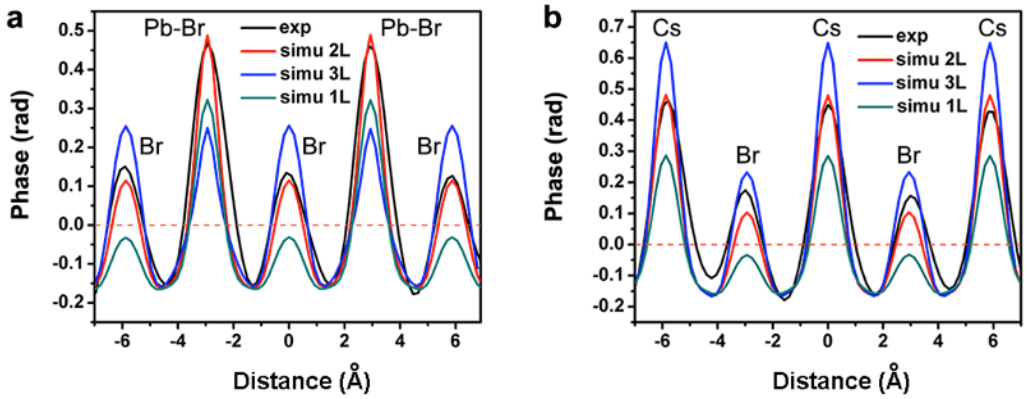

Figure S8. Comparison of experimental and simulated phase line profiles from two line scans: (a) Pb-Br and Br columns; (b) Cs and Br columns. Detailed explanation can be referred to Fig. 2 and the main text. Apart from showing experimental (black) and simulated 2-layer (red) results as in Fig.2, here, the simulated results of 1-layer (green) and 3-layer (blue) are also shown for comparison. For Cs and Br columns, the phase values increase with thickness. However, the phase of Pb-Br column begins to decrease as the thickness increases to 3-layer, as the extinction distance for the heavier Pb-Br column is shorter compared to the other two columns. It can be seen that only 2-layer model agrees well with the experimental data, further confirming the double-layer thickness of the corresponding NS.

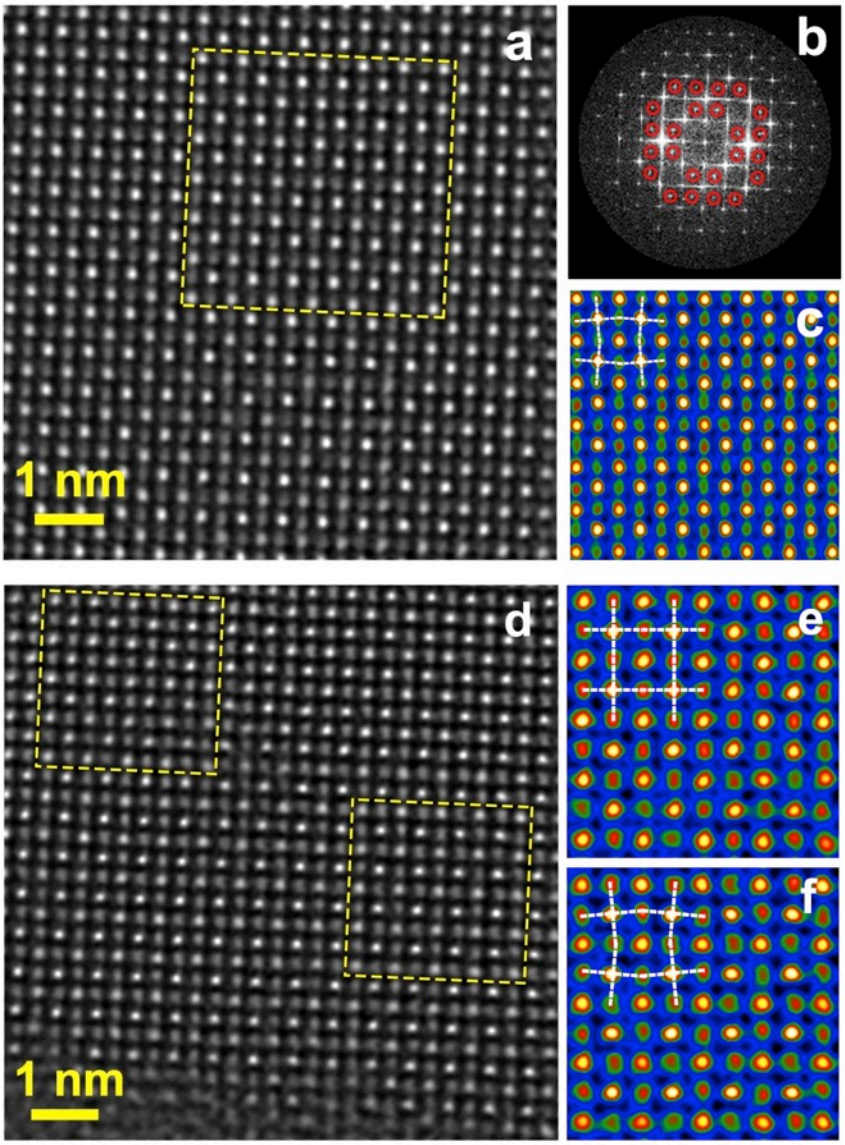

Figure S9. Orthorhombic structure of $CsPbBr_3$ NSs. (a) Atomically resolved phase image of a 2D $CsPbBr_3$ NS obtained by reconstructing 70 low dose-rate (dose-rate ~70 $eÅ^{-2}s^{-1}$) AC-HRTEM images. (b) Fourier transform of the exit-wave, which corresponds to the nano-diffraction pattern, reveals the orthorhombic structure of $CsPbBr_3$. The orthorhombic characteristic spots are highlighted by red circles. (c) False colored phase image of the boxed region in (a), better showing the tilting of octahedrons. (d) Another example of coexistence of cubic and orthorhombic $CsPbBr_3$ within single NS. Atomically resolved phase image of a 2D $CsPbBr_3$ NS obtained by reconstructing 26 AC-HRTEM images (dose-rate ~480 $eÅ^{-2}s^{-1}$). (e) Enlarged false colored phase image of the upper left boxed region in (d), showing the cubic structure without octahedron tilting. (f) Enlarged false colored phase image of the lower right boxed region in (d), showing the orthorhombic structure with octahedron tilting.

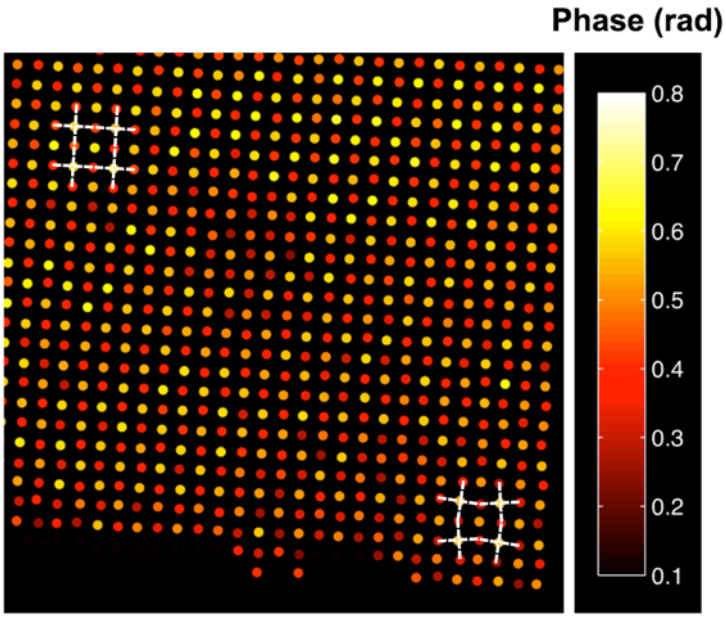

Figure S10. 2D phase mapping of Fig. S9d. Similar phase distribution is shown as in Fig. 2. Besides, from the atom column positions obtained by 2D Gaussian fitting, tilting of the octahedrons is clearly identified in the orthorhombic region.

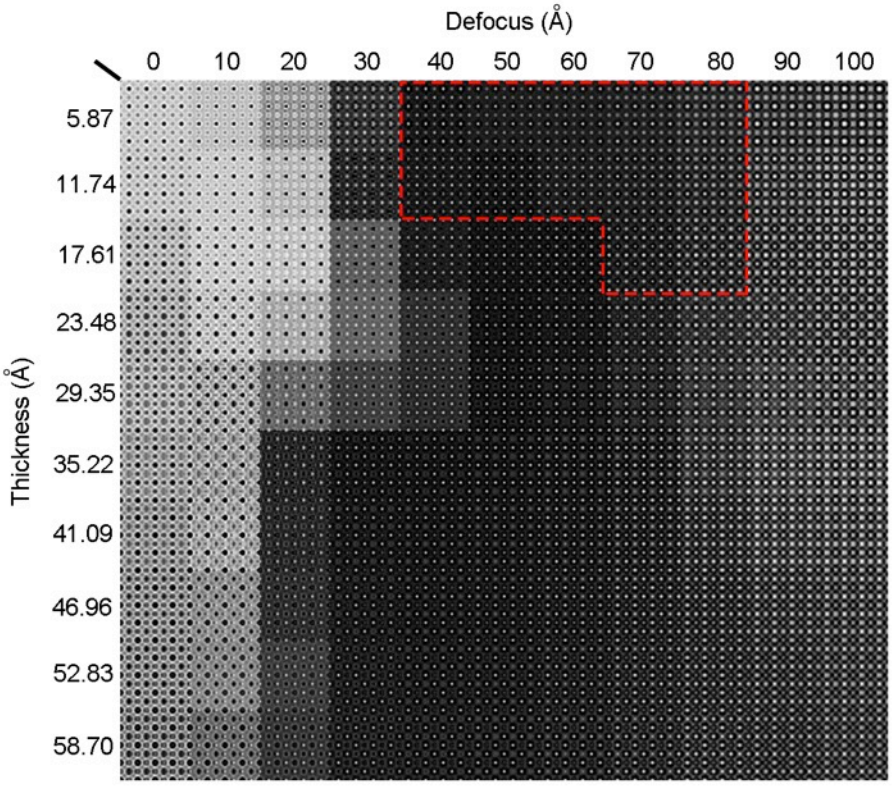

Figure S11. Simulated AC-HRTEM images under the NCSI condition, with different focus values and different crystal thickness. Here, the bulk $CsPbBr_3$ model was used. The microscope parameters used in simulation was set similar with the experimental condition. Detailed parameters are, spherical aberration C_S = -9 μm, two-fold astigmatism *A1* = 1 nm, three-fold astigmatism *A2* = 30 nm, coma *B2* = 20 nm, and vibration of 45 pm. Each image is displayed using 4 by 4 cell. Qualitatively compared with Fig. 3a, the simulated images showing best fit come from the region in red box (thickness varies from 1-layer to 3-layer). Therefore, the NS in Fig. 3a is a few-layers thick.

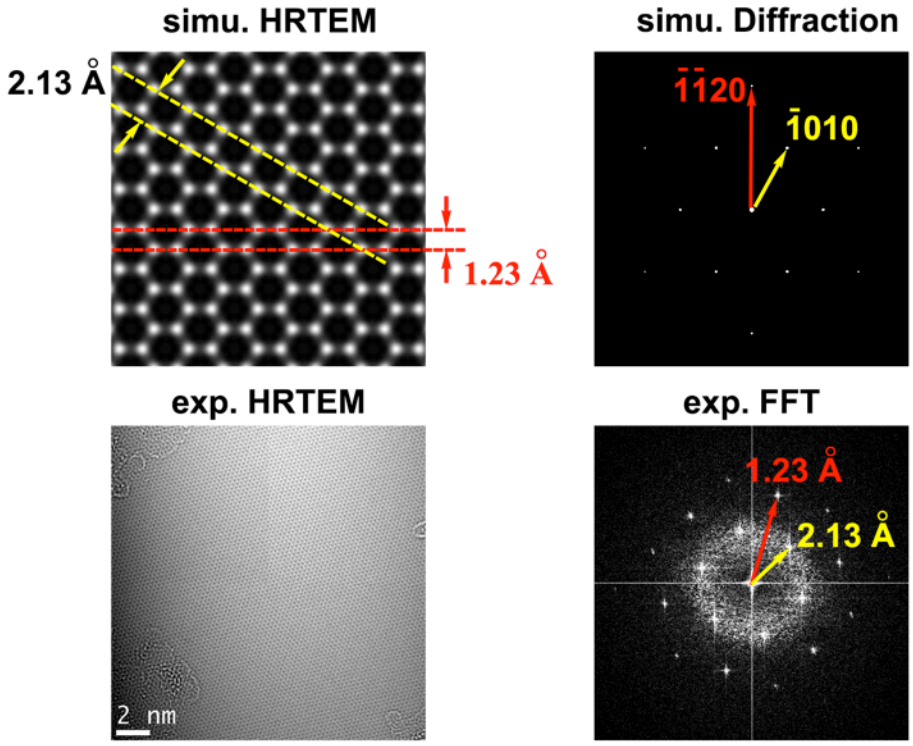

Figure S12. Lattice calibration using single-layer graphene. In order to ensure the accuracy of measurements in Fig. 4, the AC-HRTEM image has been calibrated using a graphene sample acquired at 80 kV under the same magnification.

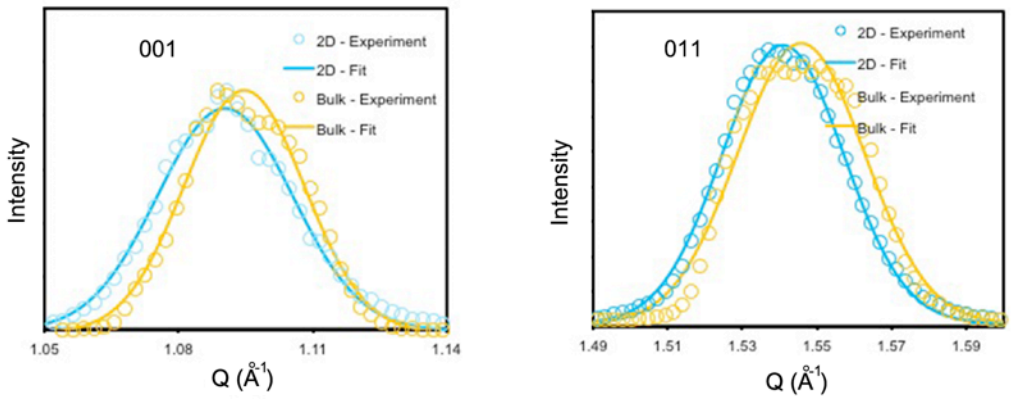

Figure S13. GIWAXS of 2D $CsPbBr_3$ NSs. {001} and {011} features of integrated GIWAXS spectra of 2D $CsPbBr_3$ NSs (in blue). Experimental data from the bulk $CsPbBr_3$ sample (in yellow) is provided for comparison. Peak shifting of 2D NSs towards lower Q value (wave vector in reciprocal space) indicates a slight lattice expansion, which is in agreement with the HRTEM measurement in Fig. 4b. A slightly lower Q-value than what is observed by TEM is likely a result from geometric and polarization factors.